Check for updates

AGU ADVANCING EARTH AND SPACE SCIENCE

Water Resources Research

RESEARCH ARTICLE
10.1029/2020WR028621

Turbulence Structure and Momentum Exchange in Compound Channel Flows With Shore Ice Covered on the Floodplains

Feifei Wang[1], **Wenxin Huai**[1], **Yakun Guo**[2], **and Mengyang Liu**[1]

[1]State Key Laboratory of Water Resources and Hydropower Engineering Science, Wuhan University, Wuhan, Hubei, China, [2]Faculty of Engineering & Informatics, University of Bradford, Bradford, UK

Key Points:

- The longitudinal evolution of the streamwise velocity in a compound channel with shore ice is presented using laboratory experiments
- The shore ice induced resistance restricts the flow development and affects the width and momentum thickness of the mixing layer
- Whether the floodplain is covered by the shore ice, the transverse momentum exchange mechanism is similar

Correspondence to:
W. Huai,
wxhuai@whu.edu.cn

Citation:
Wang, F., Huai, W., Guo, Y., & Liu, M. (2021). Turbulence structure and momentum exchange in compound channel flows with shore ice covered on the floodplains. *Water Resources Research*, *57*, e2020WR028621. https://doi.org/10.1029/2020WR028621

Received 19 AUG 2020
Accepted 11 MAR 2021

Abstract Ice cover formed on a river surface is a common natural phenomenon during the winter season in cold high latitude northern regions. For the ice-covered river with compound cross-section, the interaction of the turbulence caused by the ice cover and the channel bed bottom affects the transverse mass and momentum exchange between the main channel and floodplains. In this study, laboratory experiments are performed to investigate the turbulent flow of a compound channel with shore ice covered on the floodplains. Results show that the shore ice resistance restricts the development of the water flow and creates a relatively strong shear layer near the edge of the ice-covered floodplain. The mean streamwise velocity in the main channel and on the ice-covered floodplains shows an opposite variation pattern along with the longitudinal distance and finally reaches the longitudinal uniformity. The mixing layer bounded by the velocity inflection point consists of two layers that evolve downstream to their respective fully developed states. The velocity inflection point and strong transverse shear near the interface in the fully developed profile generate the Kelvin-Helmholtz instability and horizontal coherent vortices. These coherent vortices induce quasi-periodic velocity oscillations, while the dominant frequency of the vortical energy is determined through the power spectral analysis. Subsequently, quadrant analysis is used in ascertaining the mechanism for the lateral momentum exchange, which exhibits the governing contributions of sweeps and ejections within the vortex center. Finally, an eddy viscosity model is presented to investigate the transverse momentum exchange. The presented model is well validated through comparison with measurements, whereas the constants α and β appeared in the model need to be further investigated.

1. Introduction

Seasonal ice cover is frequently encountered in rivers located in cold regions that expose to freezing temperatures (Kirillin et al., 2012; Wazney et al., 2019), such as the Nelson River in Canada (Peters et al., 2017), the Mississippi River in America (Ettema, 2002), and the Kanas Lake in China (see Figure 1). Ice cover can have a significant impact on society and the economy. For example, the thawing of the ice cover during the spring season may result in a downstream flood, while the floating ice poses threats to hydroelectric equipment, navigation, and municipal drinking water intakes (Morse & Hicks, 2005; Zare et al., 2016). Due to its practical importance, river ice cover has attracted considerable interest from researchers in the past several decades. Teal et al. (1994) applied point-measurement methods to estimate the vertical profiles of streamwise velocity for the ice-covered channels. Muste et al. (2000) carried out laboratory experiments to determine the effect of the ice cover on the flow fields, turbulence characteristics, and sediment transport rates. Robert and Tran (2012) conducted the laboratory experiment to show that the additional ice sheet and its roughness strongly affected the vertical profiles of the Reynolds shear stresses and the turbulent kinetic energy. Ren et al. (2020) used linearized velocity potential and thin-plate elastic theory to investigate the hydroelastic waves in an ice-covered channel. Other studies of the ice-covered channel flows focused on obtaining the exact solution to the eddy viscosity (Guo et al., 2017); investigating the nonlinear interaction between a floating ice sheet and a water wave (Xia & Shen, 2002); and developing the analytical model of the transverse depth-averaged streamwise velocity distribution (Zhong et al., 2019).

The turbulence generated underneath the ice cover will inevitably interact with that generated by the roughness of the channel bed (Ettema & Zabilansky, 2004; Namaee & Sui, 2019; J. Y. Yoon et al., 1996),

© 2021. American Geophysical Union. All Rights Reserved.

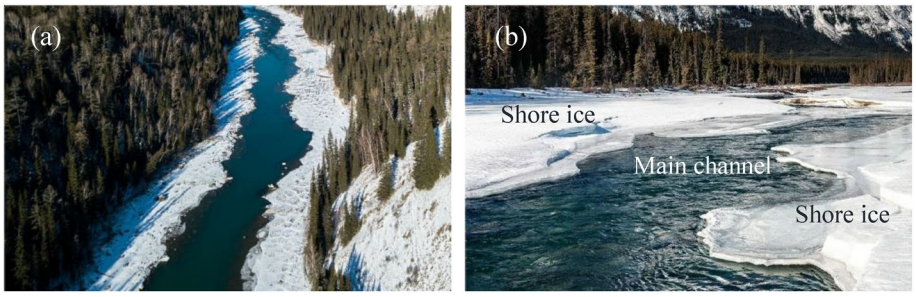

Figure 1. Example of a natural river with shore ice located at the Kanas Lake in Xinjiang, China (photograph: Zhiming Yuan & Ran Chen). (a) Aerial view of Kanas Lake; (b) Partially zoom-in view of Kanas Lake.

thereby altering the turbulent structure and affecting the lateral mass and momentum exchange in the channel flows. Literature reviews indicate that few studies have been conducted in this regard; though recently Biron et al. (2019) characterized and compared the Kelvin-Helmholtz (K-H) coherent structures within the mixing zone of a river confluence under ice-free and ice-covered conditions. So far, to the authors' best knowledge, there are hardly any investigations on the transverse mass and momentum exchange for the ice-covered compound channel flows.

Generally speaking, most natural rivers consist of shallow floodplains, transition slope regions, and a deep main channel or the so-called compound channels (Liu et al., 2013; Patel & Kumar, 2017; Proust & Nikora, 2020; Shiono & Knight, 1991). The streamwise velocity at the shallow floodplains is usually smaller than that at the deep main channel owing to the difference in flow depth and bed bottom friction (Truong & Uijttewaal, 2019). The different streamwise velocity at the floodplains and the main channel indicates that there exists the transverse velocity gradient and a mixing shear layer near the interface between the floodplains and the main channel (van Prooijen et al., 2005). The shear flow within the mixing zone can initiate the K-H instability that dominates the mixing layer dynamics and generates the horizontal coherent vortices (Proust et al., 2017; Sanjou & Nezu, 2009). The coherent vortices carry the high-momentum fluid from the main channel into the shallow floodplains, thereby enhancing the transverse scalar and momentum exchange. Previous studies show that the horizontal coherent vortices can be also detected at the confluence of two rivers (Uijttewaal & Booij, 2000; Yuan et al., 2016), in the turbulent Rayleigh-Benard convection (Chand et al., 2019), around the groynes of a trapezoidal open channel (Zhang et al., 2019), as well as in the wakes of an island (Alaee et al., 2007). Recently, Juez et al. (2019) conducted a comprehensive study in an open asymmetric compound channel to investigate the large vortical structures and mass exchange near the mixing interface under different channel characteristics. These studies indicate that the coherent vortex is probably a common characteristic in shear flows with relatively large Reynolds numbers.

When the compound channels are subjected to freezing temperature, water over the shallow floodplains is more likely to be frozen due to the slow streamwise velocity there. This means that rivers are usually covered by shore ice during the winter season, while the main channel has an ice-free water surface (see, for example, Figure 1). The presence of the shore ice can increase the frictional resistance on the floodplains and further increase the velocity gap between the shallow floodplains and the main channel (Smith & Ettema, 1997; Sukhodolov et al., 1999). This indicates that a sharp velocity transition and a strong mixing shear layer are generated across the interface. Thus, shear instability can be triggered in line with Rayleigh's theorem for inviscid parallel shear flow (White & Nepf, 2007). The development of the mixing shear layer can be restricted because of the combination of shore ice resistance and channel bed friction, while the flow field in this condition can be fully developed at a certain downstream distance (Fernandes et al., 2014). Meanwhile, the turbulence coherent structure generated underside the ice cover will compete with that generated near the channel bed, which enhances the mixing and promotes the momentum exchange (Demers et al., 2013). Nevertheless, to the best of our knowledge, there has not been reported in the published literature about the coherent structure and the transverse momentum exchange in a compound channel with shore ice cover, which motivates the present study. This study aims to obtain an insight into the turbulent flow dynamics and the momentum exchange mechanism within the mixing shear layer in a straight compound channel with ice-covered floodplains. To this end, laboratory experiments are conducted using a

Figure 2. Photograph of the experimental flume taken from downstream of the compound channel flume with shore ice.

three-dimensional (3D) SonTek Acoustic Doppler Velocimeter (ADV). As water flow develops downstream, the variation pattern of the streamwise velocity and the mixing layer width in the compound channel with and without shore ice cover are investigated using the measurements. When the water flow in the compound channel with shore ice reaches a fully developed state at a certain downstream position, a velocity inflection point and the maximum shear stress are generated at the interface between the ice-covered floodplain and the open main channel, thereby signifying the occurrence of the K-H instability. The coherent vortices that are resulted from the shear instability within the mixing layer are quasi-periodic and dominated by a single frequency. Subsequently, the dominant role of sweeps and ejections in the transverse momentum exchange between the floodplain and the main channel in the compound channel with and without shore ice cover is ascertained through the quadrant analysis of the Reynolds shear stress. Finally, although various models for predicting the transverse momentum exchange in the open compound channel flow exist (for example, van Prooijen et al., 2005), the modeling of the transverse momentum exchange in the ice-covered compound channel flows has been seldomly reported. In this study, the authors present an eddy viscosity model to simulate the transverse Reynolds shear stress for the ice-covered channel flow. The proposed model is validated using laboratory measurements.

2. Experimental Description and Methodology

The experiments are conducted in a flume of 20m length, 1m width, and 0.5 m depth, with an immobile longitudinal slope of $S_0 = 0.01\%$, at the State Key Laboratory of Water Resources and Hydropower Engineering Science in Wuhan University (see Figure 2). To reduce the effect of the inlet on the flow downstream, the horizontal PVC pipes with a diameter of 2.3 cm and a length of 1m are placed in rows at the flume inlet and form a rectifier of 1m length, 0.989 m width, and 0.46 m thick to dampen the turbulence generated at the inlet (not shown in Figure 2). The channel cross-section is symmetrical and composed of a trapezoidal main channel flanked by two floodplains. The bottom and sidewall of the flume are composed of PVC boards and Perspex glass, respectively. The water is fed from an underground circulated reservoir with a constant head by using a centrifugal pump. The water temperature, which is measured by a mercury thermometer, is about 23.5 °C. The prescribed flow discharge is measured and monitored accurately by an electromagnetic flowmeter located upstream of the flume. The desired flow depth is maintained by an adjustable tailgate mounted at the downstream end of the flume. The water-surface elevation is measured by point gauges installed on the instrument carriage. The shore ice is simulated by plastic foam boards, whose surface's Manning roughness n is about 0.0105 (Chow, 1959), which is slightly rougher than the bottom of the flume. The plastic foam board is 1m in length and 0.2 m in width and is interlocked together to form continuous floating shore ice. The flow velocity field is measured using a three-dimensional (3D) SonTek Acoustic Doppler Velocimeter (ADV). These measured velocities are used to investigate the turbulence structure and transverse momentum exchange between the ice-covered floodplain and the main channel in this study.

To compare and evaluate the effect of the shore ice cover on the flow field, we have conducted laboratory experiments with and without the shore ice cover. Figure 3 shows the sketch of the plan view and cross-section of the experimental compound channel with shore ice. At the entrance of the measurement section, whether the compound channel is covered by the shore ice, two PVC splitter plates with a length of 1m are symmetrically arranged at the two interfaces between the main channel and the floodplains, for allowing the water flow to develop independently within their respective zone and reducing the transverse mass transfer owing to flow adjustment. Thus, under the combined action of the rectifier at the flume inlet and the splitter plates, the uniform flow condition will be realized in a short longitudinal distance from the inlet. The shore ice in the measurement section is 12m long and symmetrically covered the left and right floodplains. The width of each side floodplain is $B_f = 0.20$ m, while the side slope is $s = 1$. Half the width of the

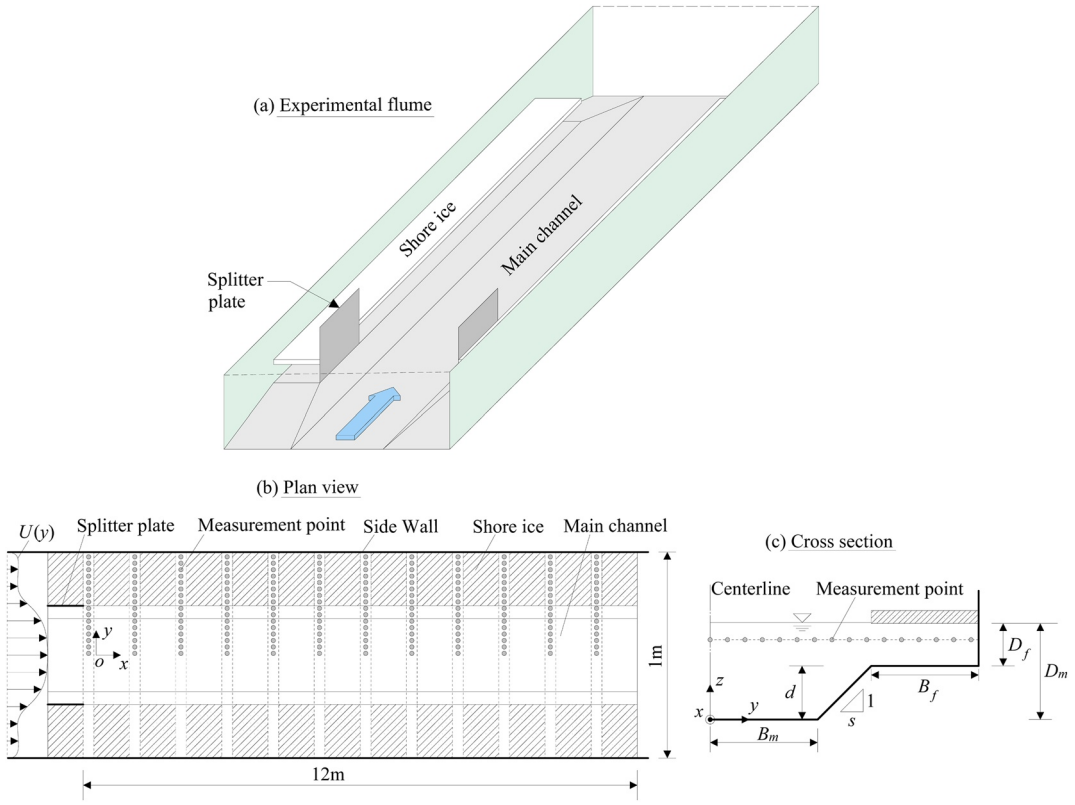

Figure 3. Sketches of the plan view (b) and the cross-section (c) of the experimental flume (a).

main channel is $B_m = 0.20$ m. The main channel bankfull height, namely from the main channel bottom to the floodplain bottom, is $d = 0.10$ m.

The Cartesian coordinate system x, y, and z axes refer to the longitudinal (i.e., along the channel bed bottom), lateral, and vertical (i.e., normal to the channel bed bottom) directions, respectively. The positive directions of x, y, and z axes point downstream of the water flow, to the left floodplain (looking downstream), and to the water surface, respectively (see Figure 3c). The system origin is $x = 0$ at the leading edge of the measurement section, $y = 0$ at the channel center, and $z = 0$ at the main channel bed bottom. In this coordinate system, (u, v, w), (U, V, W), and (u', v', w') denote the instantaneous velocity, time-averaged velocity, and instantaneous velocity fluctuations in the x, y, and z directions, respectively.

Given the symmetry of the experimental setup, measurements are mostly taken on the left-hand half of the channel. The instantaneous velocity is measured using the SonTek 16-MHz ADV equipped with the 3D up-looking probe. The sampling rate of the ADV is 50 Hz with the sampling volume being 0.09 cm^3. The distance to the sampling volume is 5 cm and the sampling time duration is 160s (i.e., 8,000 samplings). The velocity range is ±100 cm/s with a resolution of 0.01 cm/s. To achieve high-resolution measurements, the correlation coefficient that is larger than 80% and the signal-to-noise ratio (SNR) is greater than 15 dB is adopted here. As such, the inferior samples (correlation coefficient < 80% and SNR < 15 dB) are removed. The measured data are then filtered by using Tukey's method (Goring & Nikora, 2002). The measurement cross-sections are located at downstream positions from $x = 0$ m to $x = 11$ m with a longitudinal spacing of 1 m, as shown in Figure 3b. At each measurement cross-section, at least 25 measurement points are transversely arranged. For the compound channel with shore ice, the measurement points are located at the water level corresponding to four-fifths of the floodplain flow depth. This measurement pattern indicates that the distance from the measurement point to the water surface is equal to one-fifth of the ice-covered floodplain flow depth. Thus, all measurement points are on the same horizontal plane. The averaged relative error between the time-averaged streamwise velocities measured at the water level of the four-fifths of the ice-covered floodplain flow depth (denoted by $U_{4d/5}$) and the depth-averaged streamwise

Table 1
Experimental Parameters

Case	Q (m^3/s)	D_f (m)	D_m (m)	D_r (−)	$U_{B\text{-}f}$ (m/s)	$U_{B\text{-}m}$ (m/s)	Fr_f (−)	Fr_m (−)	Re_f (−)	Re_m (−)	n_b (−)	n_i (−)	Note
I	0.0306	0.10	0.20	0.5	0.139	0.215	0.140	0.160	5,979	37,249	0.009	0.0105	Cover
II	0.0411	0.15	0.25	0.6	0.155	0.218	0.128	0.144	9,076	48,137	0.009	0.0105	Cover
III	0.0420	0.15	0.25	0.6	0.178	0.219	0.147	0.145	16,438	48,311	0.009	-	Open

velocities (denoted by U_d) is below 10% (for more details, see Appendix A). Hence, $U_{4d/5}$ is used to replace U_d in the compound channel flow with the shore ice and is hereafter denoted as U for brevity and convenience. For the open compound channel without shore ice, the measurement points are located at the water level corresponding to the mid-depth of the floodplain (White & Nepf, 2007). To achieve the velocity measurements beneath the shore ice, the shore ice in the front of the measurement cross-section will be disconnected from the shore ice in the back of the measurement cross-section. The width of the separation is set at 0.9 cm considering that the diameter of the measurement stem of the 3D up-looking probes is 0.7 cm. Moreover, due to the configuration of the 3D up-looking probe, the minimum allowable flow depth of the ice-covered floodplain is 10 cm. Thus, we perform three cases in the compound channel with and without shore ice.

Table 1 shows the experimental conditions. Cases I and II with different flow depths are carried out in the compound channel with shore ice covered on the floodplains. Case III with the same flow depth as that of Case II is performed without the shore ice covered on the floodplains. In Table 1, Q is the total flow discharge of the compound channel, D is the flow depth, D_r denotes the flow depth ratio and $D_r = D_f / D_m$, and U_B is the longitudinal bulk flow velocity. The Reynolds number is calculated as $Re = U_B R/\nu$ where R and ν are the hydraulic radius and the water kinematic viscosity, respectively. The Froude number is computed as $Fr = U_B / \sqrt{gA / B}$ where g, A, and B are the gravitational acceleration, the area of the calculated region, and the total width of the calculated region, respectively. n_b and n_i are Manning's roughness coefficients of the channel bed and the shore ice, respectively. Subscripts m, f, b, and i refer to the main channel, the floodplain, the channel bed, and the ice cover, respectively. As aforementioned, the channel bed is made up of PVC boards with a smooth surface. The shore ice consists of close-grained plastic foam boards. Therefore, according to Chow (1959) and Hoque (2009), the values of n_b and n_i are given as 0.009 and 0.0105, respectively.

3. Experimental Results

3.1. Longitudinal Development of the Water Flow

Figure 4 shows the longitudinal development of the transverse profile of the streamwise velocity. For Cases I and II, the streamwise velocity in the main channel (i.e., $0 \le y \le 0.2$ m) increases initially with the downstream distance and finally reaches the fully developed state at approximately $x = 3$m and $x = 4$m, respectively. The streamwise velocity at the ice-covered floodplain (i.e., $y \ge 0.3$ m) for Cases I and II decreases with the increase of the downstream distance and reaches the fully developed state at approximately $x = 6$m and $x = 7$m, respectively. For Case III (i.e., the open compound channel without the shore ice covered on the floodplain), the longitudinal evolution of the streamwise velocity U has a similar trend to that of the compound channel with the shore ice. Comparing Cases III with II, the streamwise velocity U in the main channel for Case III also reaches the fully developed state at about $x = 4$m; whereas the streamwise velocity U at the floodplain for Case III needs a longer longitudinal distance (i.e., $x = 8$m) to achieve the fully developed state. Meanwhile, it is noted that there is a weak shear layer in the streamwise velocity profile when $0.42\text{ m} \le y \le 0.45$ m for Case III reflecting the influence of the vertical wall boundary resistance, which differs from that for Cases I and II. This different result may be ascribed to the fact that the shore ice covered on the floodplains for Cases I and II has an inhibition effect on the water flow development near the vertical wall boundary. Figure 4 also signifies, whether the floodplain is covered by the shore ice, the flow discharge of the floodplain upstream of the fully developed profile exceeds the flow discharge corresponding to the uniform flow. Accordingly, as the water flow develops downstream, a transverse mass and momentum

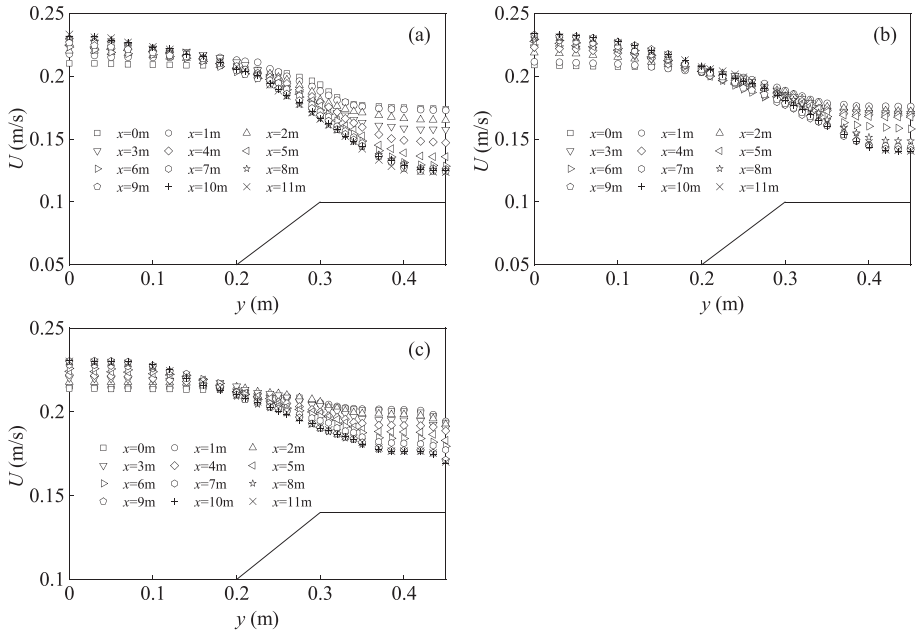

Figure 4. Lateral distribution of the streamwise velocity developing downstream from the splitter plates. (a) Case I; (b) Case II; (c) Case III.

transfer takes place from the floodplain into the main channel, which increases the streamwise velocity in the main channel and decreases the streamwise velocity at the floodplain. Moreover, due to the existence of the shore ice, the velocity difference between the main channel and the ice-covered floodplain for Cases I and II is greater than that for Case III, indicating that the velocity gradient for Cases I and II is larger than that for Case III and hence a stronger shear layer exists near the interface for the compound channel with the shore ice. Thus, from the visualization perspective, the longitudinal uniformity of the water flow for the three cases has been realized, which is subsequently verified by analyzing the mixing layer evolution.

The transverse profile of the streamwise velocity with an inflection point is asymmetrical as the velocity at the floodplain rapidly decreases while the velocity in the main channel decreases gradually. Meanwhile, given that the inflection point is mainly responsible for flow instability, the mixing layer is divided into two layers, namely the main channel and the floodplain mixing layers, bounded by the velocity inflection point. Figure 5 is a schematic plot of U to describe the two mixing layers. The widths of the main channel and the ice-covered floodplain mixing layers are denoted as δ_m and δ_f, respectively, and can be obtained as follows (Dupuis et al., 2017):

$$U\left(y_{IP} - \delta_m / 2\right) = \frac{U_2 + U_{IP}}{2} \tag{1}$$

$$U\left(y_{IP} + \delta_f / 2\right) = \frac{U_1 + U_{IP}}{2} \tag{2}$$

where U_1 is the streamwise velocity deep inside the floodplain region, U_2 denotes the maximum streamwise velocity outside the mixing layer in the main channel, U_{IP} is the streamwise velocity at the inflection point, and y_{IP} is the inflection point position. In this study, the measured position of the inflection point y_{IP}, which appears constant and is independent of the flow depth and the channel length, is near the interface with an absolute error of 1 cm. Thus, y_{IP} is consistent with the interface location. Consequently, the total width of the mixing layer can be obtained as $\delta_{tot} = \delta_m + \delta_f$.

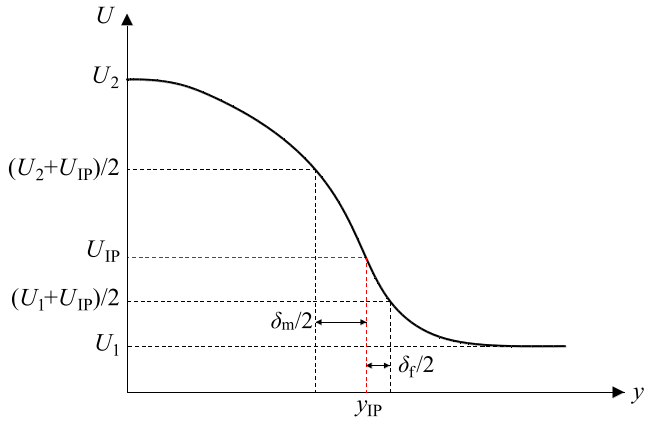

Figure 5. Sketch the streamwise velocity profile, definition of the mixing layer, and related variables.

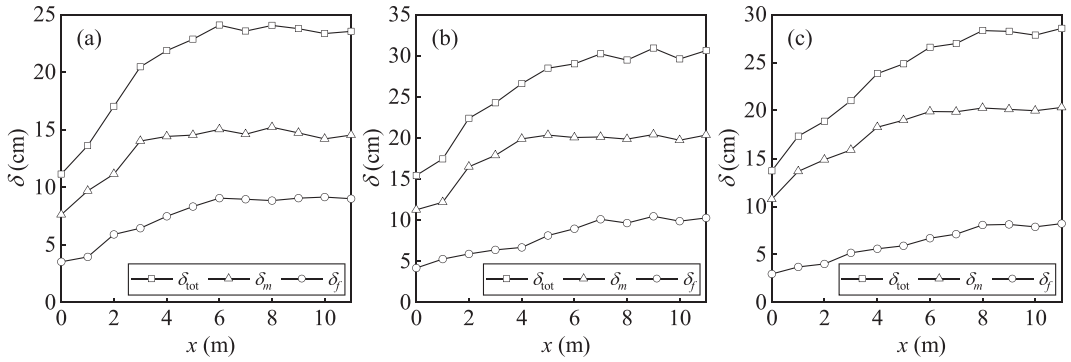

Figure 6. Longitudinal evolution of the mixing layer width for Cases I (a), II (b), and III (c).

Figure 6 shows the longitudinal evolution of the mixing layer width. For Cases I and II, the main channel mixing layer widths increase along with the longitudinal distance and then level off at $x = 3$m and $x = 4$m, respectively, while the ice-covered floodplain mixing layer widths need longer downstream distances (i.e., $x = 6$m and $x = 7$m for Cases I and II, respectively) to approach the stabilized state. By combining the stabilized distance required for the main channel mixing layer with that for the ice-covered floodplain mixing layer, the total mixing layer widths for Cases I and II reach the stable state at $x = 6$m and $x = 7$m, respectively. From Figure 6c, the evolution trend of the mixing layer for Case III is similar to that in the compound channel with the shore ice. Comparing with Case II, the main channel mixing layer for Case III needs approximately the same distance to reach stabilization. Nonetheless, due to the lack of shore ice restriction, the floodplain mixing layer for Case III takes a relatively long distance (i.e., $x = 8$m) to achieve stabilization. These results indicate that the three cases achieve longitudinal uniformity at a certain distance, which is consistent with the experimental results on streamwise velocity. Although the determination of the mixing layer width presented here exhibits some difference from the previous mixing layer definition (White & Nepf, 2007), the mechanism is similar.

Given the presence of the mixing shear layer, the transverse momentum exchange occurs near the interface between the floodplain and the main channel. The momentum thickness of the mixing shear layer θ is calculated as (White & Nepf, 2007):

$$\theta = \int_{-\infty}^{+\infty} \left\{ \frac{1}{4} - \left[\frac{U - (U_1 + U_2)/2}{U_2 - U_1} \right]^2 \right\} dy \tag{3}$$

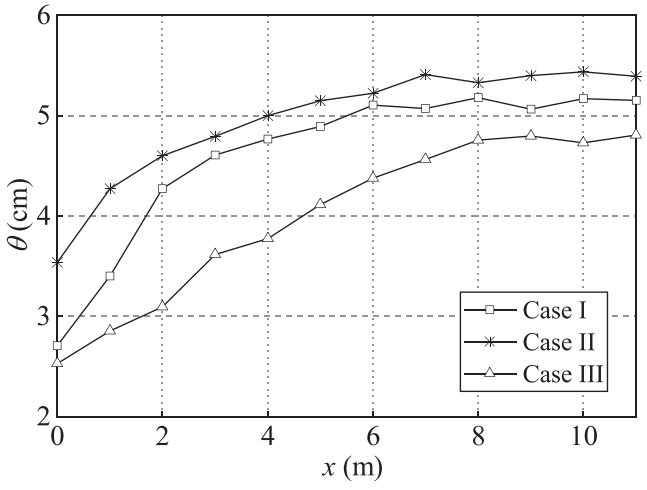

Figure 7. The development of the momentum thickness for the three cases.

Figure 7 shows that the momentum thickness steadily increases with the increase of the longitudinal distance and then oscillates around a certain value for the three cases. The momentum thickness of Case I reaches an asymptotic stable value (i.e., 5.1 cm) for longitudinal distance $x \geq 6$m, while for Case II, its momentum thickness approaches a steady value (i.e., 5.4 cm) after $x \geq 7$m. For Case III, the momentum thickness reaches the stabilization when $x \geq 8$m, and has a steady value of 4.8 cm. It is worth noting that the momentum thickness for Case II is greater than that for Case III, implying that the momentum loss in Case II is larger than that in Case III. This result may be ascribed to the fact that the presence of the shore ice adds the frictional resistance on flow at the floodplains, thereby increasing the momentum cost in Case II. Therefore, from the development of the streamwise velocity and the mixing layer, it can be concluded that the water flow for the three cases reaches the longitudinal uniformity at a certain downstream position, and the existence of the shore ice induces a relatively strong shear layer and restricts the longitudinal evolution of the mixing shear layer.

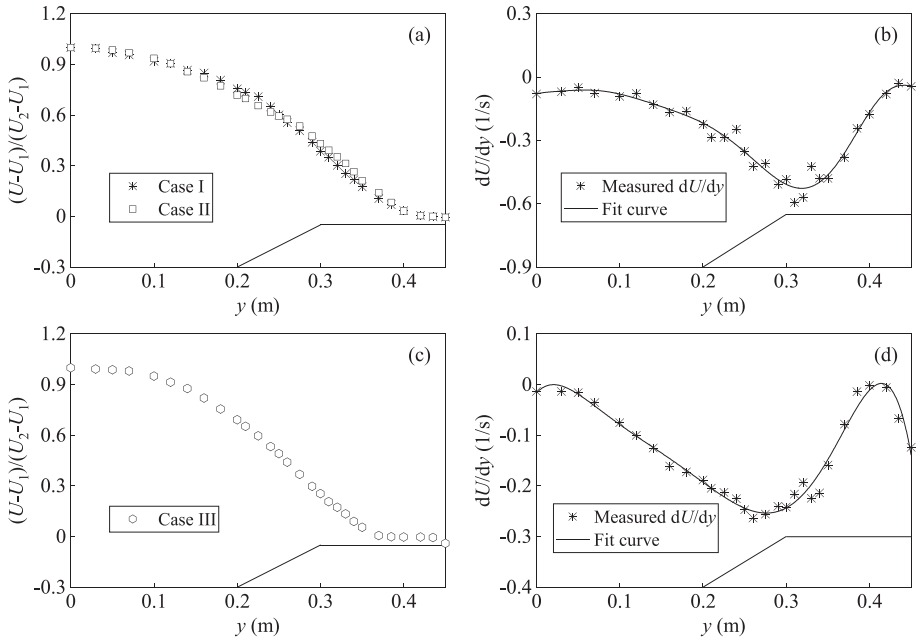

Figure 8. Measured streamwise velocity and velocity gradient profiles at the representative fully developed cross-section for Cases I (a–b), II (a), and III (c–d).

3.2. Fully Developed Streamwise Velocity Profiles and the Reynolds Shear Stress

Figure 8 shows the transverse distributions of the streamwise velocity and velocity gradient measured at the representative fully developed cross-section. It is seen that the lateral profiles of the streamwise velocity for Cases I and II are self-similar. Specifically, the streamwise velocity decreases sharply near the edge of the ice-covered floodplain, while a gradual decrease of the streamwise velocity occurs in the main channel. This indicates that an inflection point exists in the streamwise velocity profile at the interface between the ice-covered floodplain and the main channel. For Case III, the streamwise velocity has a similar variation trend in the lateral direction. Unlike Cases I and II, the streamwise velocity for Case III outside the floodplain mixing layer (i.e., 0.42 m $\leq y \leq$ 0.45 m) still decreases, manifesting the influence of the vertical wall boundary resistance. These results reveal that the presence of the shore ice may suppress the flow development near the vertical wall boundary. To illustrate the existence of the velocity inflection point, we calculate the velocity gradient dU/dy for Cases I and III, as shown in Figures 8b and 8d. It is observed that the velocity inflection point for Case I appears at the edge of the ice-covered floodplain, whereas the velocity inflection point for Case III deviates from the interface and takes place at the side slope domain.

The fully developed transverse profiles of the Reynolds shear stress for the three cases are plotted in Figure 9. It is seen that the Reynolds shear stress has negative values and presents a similar transverse variation trend to that of the velocity gradient, which is decided by the coordinate system prescribed in this study and is consistent with Prandtl's mixing-length theory. For Cases I and II, the Reynolds shear stress is near zero outside the mixing layer, indicating that there is little transverse momentum exchange taking place in this region. Within the mixing layer, the Reynolds shear stress is relatively large, thereby facilitating the transverse momentum exchange between the main channel region and the ice-covered floodplain region. Meanwhile, a maximum Reynolds shear stress exists near the interface, which is consistent with the position of the velocity inflection point. Thus, according to Rayleigh's theorem, the presence of the velocity inflection point and the relatively strong shear near the interface for Cases I and II may result in the K-H instability and hence the coherent oscillations. Differing from Cases I and II, the maximum Reynolds shear stress for Case III deviates from the interface to the side slope, and there exists the momentum exchange outside the floodplain mixing layer. This deviation for Case III may be caused by the relatively large flow depth ratio and the lack of shore ice inhibition. Although the maximum Reynolds shear stress and the

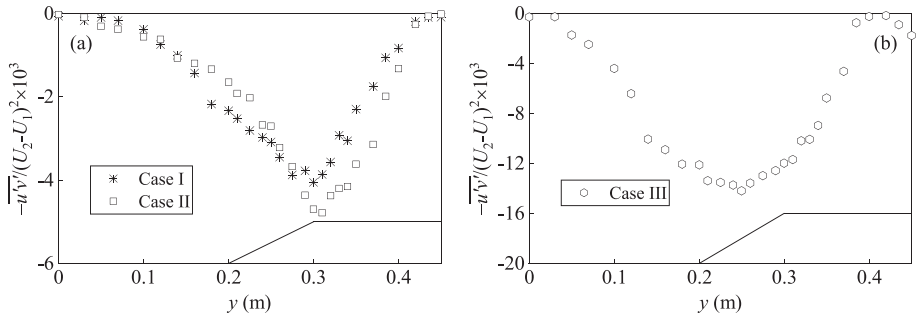

Figure 9. Fully developed lateral profile of the Reynolds shear stress. (a) Cases I and II; (b) Case III.

velocity inflection point for Case III diverge from the interface, their positions are approximately consistent, implying the occurrence of the coherent oscillations to some extent.

3.3. Coherent Fluctuations and Turbulence Structures

Regular coherent vortices formed in the mixing layer, which are responsible for the turbulent shear stress, endow the velocity time series with coherence and periodicity. As coherent vortices develop along the edge of the ice-covered floodplain, typical flow events (i.e., sweeps, inward interactions, ejections, and outward interactions) occur simultaneously. Figure 10 shows the typical time series of the instantaneous streamwise velocity u, transverse velocity v, and the Reynolds shear stress $u'v'$ at the interface (i.e., within the vortex center, $y = 0.30$ m) and outside the mixing layer (i.e., outside the vortex center, $y = 0.42$ m) for Cases II and III. In Figure 10, both the transverse velocity $v(t)$ and the Reynolds shear stress $u'v'(t)$ is shifted for the sake of clarity. The dot-dashed lines of $u(t)$ and $v(t)$ refer to their respective time-averaged values, whereas the dot-dashed line of $u'v'(t)$ denotes its shifted value. From Figures 10a and 10c, the streamwise velocity fluctuation u' and the transverse velocity fluctuation v' inside the vortex core for Cases II and III are positively correlated, implying that the momentum transport event takes place. The time series of $u'v'(t)$ shows that sweeps (Sw)

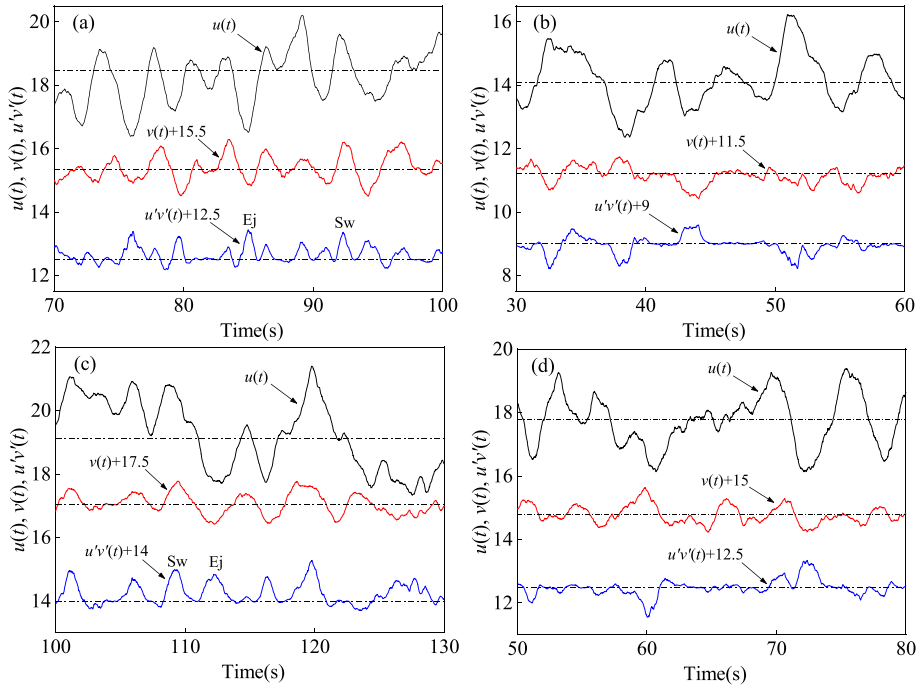

Figure 10. Typical time series of the instantaneous streamwise velocity u, transverse velocity v, and the Reynolds shear stress $u'v'$ at the interface (i.e., $y = 0.30$ m) and outside the mixing layer (i.e., $y = 0.42$ m) for Cases II (a–b) and III (c–d).

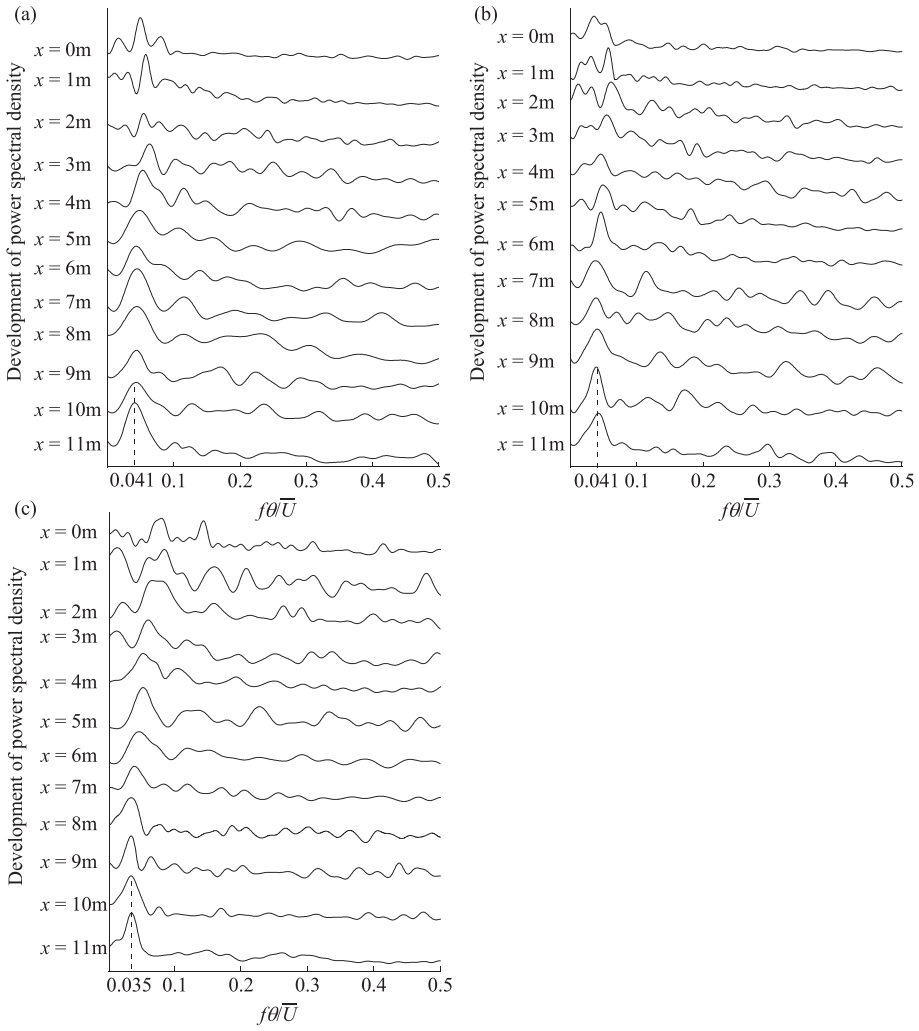

Figure 11. Power spectral density of the transverse velocity fluctuation $v'(t)$ at the interface that evolves downstream from the splitter plate. (a) Case I; (b) Case II; (c) Case III.

occur when $u' > 0$ and $v' > 0$, indicating that the lateral momentum penetrates from the main channel region into the floodplain region. It is seen that the ejections (Ej) occur when $u' < 0$ and $v' < 0$, indicating that the momentum within the floodplain domain flows out into the main channel domain. Hence, a relatively large time-averaged Reynolds shear stress $\overline{u'v'}$ resulted from the lateral momentum transport events is captured near the interface. Comparing Figure 10a with Figure 10c, it can be also found that the fluctuation frequency for Case II is larger than that for Case III, indicating that the presence of the shore ice increases the intensity of the turbulent vortex. Figures 10b and 10d show that the velocity fluctuations of $u(t)$ and $v(t)$ outside the mixing layer are weakly correlated, and the time-averaged Reynolds shear stress $\overline{u'v'}$ is approximately equal to zero. It can be inferred that the positive and negative momentum fluxes cancel each other out. Notably, the velocity fluctuations inside the vortex center are quasi-periodic, suggesting the existence of a unitary dominant frequency. Therefore, the governing frequency can be identified by utilizing the following spectral analysis.

Figure 11 shows the power spectral density of the transverse velocity fluctuation at the interface of different longitudinal positions for the three cases. In Figure 11, the frequency f is normalized using the local time-averaged streamwise velocity $\overline{U}$ (i.e., $\overline{U} = \left(U_1 + U_2\right)/2$) and the corresponding momentum thickness θ, forming a dimensionless frequency $f\theta / \overline{U}$ (i.e., the Strouhal number). At the channel upstream, such as $x \le 3$m, the power spectra for the three cases present three or more peaks (e.g., Figures 11a $x = 0$m; Figures 11b $x = 2$m; Figures 11c $x = 1$m), indicating the presence of the diverse energy modes. As the water flow evolves downstream, the fully developed states of the power spectra for the three cases

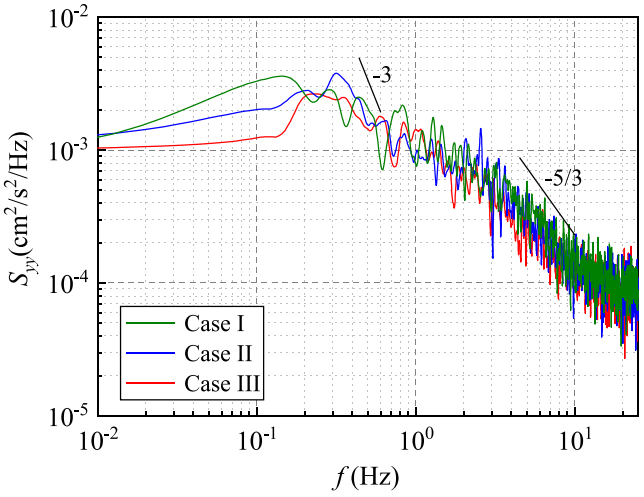

Figure 12. Power spectral densities of the transverse velocity fluctuation $v'(t)$ at the interface of the representative fully developed cross-section for the three cases.

are reached at x = 6m, x = 7m, and x = 8m, respectively. Simultaneously, the energy converges to a constant mode, which corresponds to the dominant frequency of the coherent vortical structure. The dominant dimensionless frequency $f\theta / \bar{U}$ for Cases I and II is approximately 0.041 with a deviation of ±0.003, whereas the dimensionless frequency $f\theta / \bar{U}$ for Case III is about 0.035 which is slightly smaller than that for Cases I and II.

Figure 12 shows the power spectral density of the transverse velocity fluctuation $v'(t)$ against the signal frequency f at the interface of the representative fully developed cross-section for the three cases. It is seen that the power spectral density S_{yy} for the three cases decreases progressively in the high-frequency region and approximately follows a descending law of −5/3 power, which is similar to the Kolmogorov spectrum. The momentum transportation here is dominated by the inertia force, while the influence of the viscous force can be ignored. Furthermore, the power spectra for the three cases have definite peaks near the middle range of the signal frequency, and then gradually decrease with a slope of −3. This indicates the existence of a quasi-2D turbulence coherent structure (Proust et al., 2017). Meanwhile, the peak value of the power spectral for Case III is smaller than that for Case II, indicating that the turbulent vortex for Case III is weaker. It is also seen that the turbulent vortex for Case III oscillates slower when compared with that for Case II, which is consistent with the results shown in Figure 10. Thus, it can be inferred that the existence of the shore ice enhances the oscillation and strength of the turbulent vortices.

3.4. Quadrant Analysis of the Transverse Momentum Exchange

The quadrant analysis of the Reynolds shear stress is a typical and reliable turbulence data processing technique that can provide interior and pivotal information about the momentum exchange mechanism for various flow events. According to the coordinate system defined in this study, the four quadrants of the u'-v' plane associated with four flow events are classified as sweeps ($u' > 0$, $v' > 0$), inward interactions ($u' < 0$, $v' > 0$), ejections ($u' < 0$, $v' < 0$), and outward interactions ($u' > 0$, $v' < 0$). Willmarth and Lu (1972) concentrated on intense Reynolds shear stress and proposed the hole concept for the u'-v' plane, which extended the application of the quadrant analysis. The hole domain consists of a set of hyperbolic curves in each quadrant that corresponds to $\left|u'v'\right| = H \cdot \left|\overline{u'v'}\right|$, where H is a given threshold value and $\overline{u'v'}$ is the averaged value of the product of the streamwise velocity fluctuation u' and the transverse velocity fluctuation v'. Thus, the contribution of the Reynolds shear stress in each quadrant outside the hole to the total Reynolds shear stress can be determined. Case I is used as an example to illustrate the quadrant analysis technique in this study. Figure 13 shows the quadrant distribution of (u', v') measured at the interface of the representative fully developed cross-section for Case I. It can be observed that the dominant flow events outside the hole are in Q1 and Q3, indicating that the transverse momentum exchange at the interface is mediated by sweeps and ejections. Given the prominent role of sweeps and ejections, substantial momentum flux and strong shear are generated at the edge of the ice-covered floodplain.

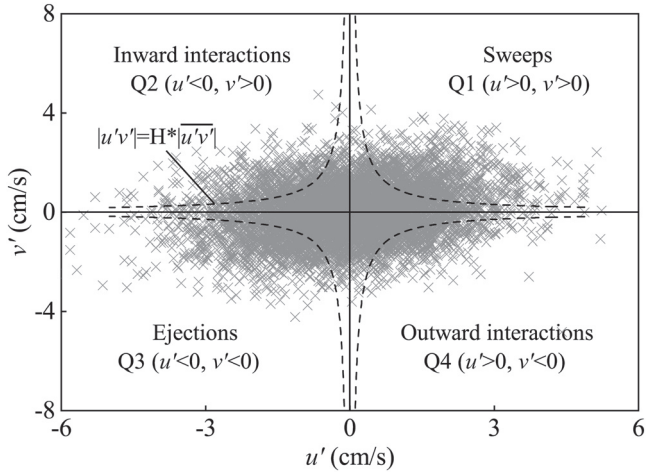

Figure 13. Quadrant distribution of (u', v') measured at the interface of the representative fully developed cross-section for Case I with H = 3. The dashed lines in the figure refer to the hyperbolic curves corresponding to $\left|u'v'\right| = H \cdot \left|\overline{u'v'}\right|$.

The contribution of the flow events in each quadrant to the Reynolds shear stress with a given threshold value H is expressed as (Lu & Willmarth, 1973):

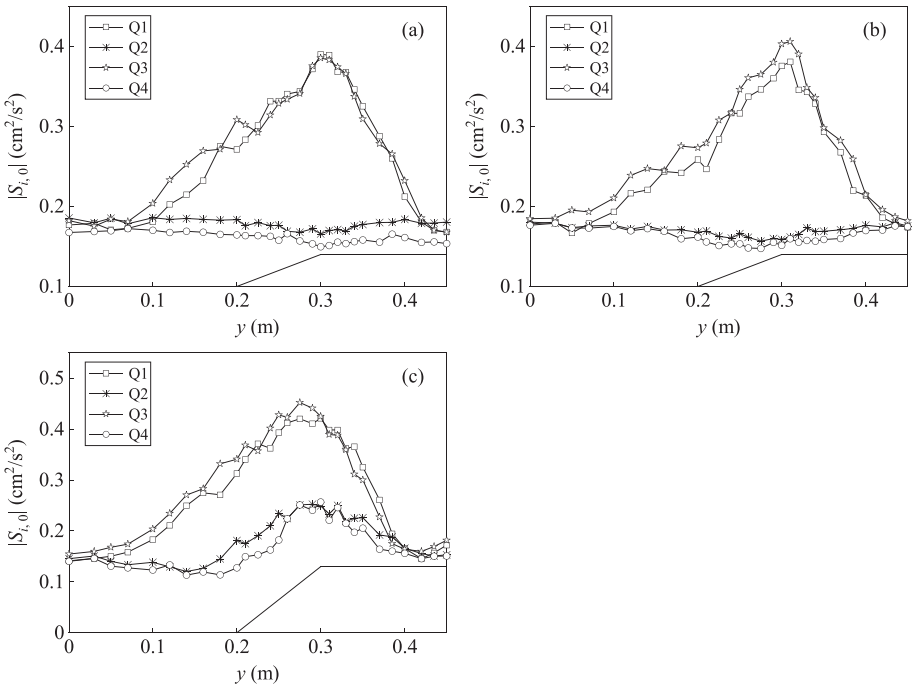

Figure 14. Transverse distributions of the contributions in each quadrant to the Reynolds shear stress with the threshold value $H = 0$ at the representative fully developed cross-section for Cases I (a), II (b), and III (c).

$$S_{i,H} = \frac{1}{T}\int_0^T C_{i,H}(t)u'(t)v'(t)dt \tag{4}$$

where $S_{i,H}$ is the contribution value in the ith quadrant; i is an integer, and $i \in [1,4]$; T is the sampling time; and $C_{i,H}$ is a constant defined as:

$$C_{i,H} = \begin{cases} 1, \left|u'(t)v'(t)\right| > H\left|\overline{u'v'}\right| \text{ and } \left(u'(t), v'(t)\right) \text{locates in the } i\text{th quadrant} \\ 0, \text{otherwise} \end{cases} \tag{5}$$

Given that the sign of $S_{i,H}$ in Q2 and Q4 is negative, we investigate the absolute value of the contribution $S_{i,H}$ (i.e., $|S_{i,H}|$). Figure 14 presents the transverse distribution of the contribution $|S_{i,H}|$ in each quadrant to the Reynolds shear stress when $H = 0$ for the three cases. It is seen that sweeps (Q1) and ejections (Q3) are the dominant flow events that make the major contributions to the transverse momentum exchange within the mixing layer (i.e., 0.1 m $< y <$ 0.4 m). Outside the mixing layer (i.e., $y <$ 0.1 m and $y >$ 0.4 m), the contributions in the four quadrants for Cases I and II have nearly the same magnitudes, indicating that the positive momentum flux is canceled out by the negative momentum flux. For Case III, however, there still exists lateral momentum exchange outside the floodplain mixing layer. This is because the contributions in Q1 and Q3 are slightly larger than that in Q2 and Q4 when $y >$ 0.4 m. By comparing Figure 14b with Figure 14c, it is clear that the impacts of inward interactions (Q2) and outward interactions (Q4) near the interface for Case III are stronger than those for Case II. This may be caused by the lack of shore ice suppression in the water flow for Case III. Furthermore, in light of the predominant role of sweeps and ejections, the lateral variation trends of sweeps and ejections for the three cases are similar to those of the absolute Reynolds shear stress. Meanwhile, within the floodplain mixing layer (i.e., 0.3 m $< y <$ 0.4 m), sweeps and ejections have almost the same contributions to the Reynolds shear stress. In the main channel mixing layer (i.e., 0.1 m $< y <$ 0.3 m), the contribution of ejections slightly outweighs that of sweeps. These results indicate that sweeps transport high-momentum flow toward the floodplain, while ejections subsequently convey the

high-vorticity flow from near the interface back into the main channel, thereby completing the momentum exchange between the floodplain and the main channel.

4. Modeling of the Transverse Momentum Exchange

From the experimental results discussed above, the dominant contribution to the transverse momentum exchange is the turbulent Reynolds shear stress. Though the advective dispersion in the compound channel flows also enhances the lateral momentum transport, its contribution is relatively small compared with that from the Reynolds shear stress for most flow conditions (van Prooijen et al., 2005). Therefore, the total momentum exchange between the ice-covered floodplain and the main channel is assumed to come from the turbulent Reynolds shear stress, namely $\overline{T_{xy}} \approx -\rho\overline{u'v'}$ where $\overline{T_{xy}}$ denotes the time-averaged transverse shear stress.

To model the transverse shear stress, the eddy viscosity concept or the Boussinesq approach is often employed:

$$\overline{T_{xy}} \approx -\rho\overline{u'v'} = \rho\nu_t \frac{dU}{dy} \tag{6}$$

where ν_t represents the eddy viscosity. Thus, the determination of a proper eddy viscosity model is the key point to accurately simulate the transverse momentum exchange. Following the concept of van Prooijen et al. (2005) regarding the eddy viscosity model, an eddy viscosity model is proposed in this study for the ice-covered compound channel flows. Similarly, the eddy viscosity ν_t ($\nu_t = \nu_t^{'} + \nu_t^{'}$) consists of two isolated components, namely, the eddy viscosity caused by the turbulence that is generated underside the ice cover and on the channel bed bottom ($\nu_t^{'}$) and the eddy viscosity resulted from the horizontal coherent structures ($\nu_t^{'}$). Considering the underlying mechanisms of the two eddy viscosity components, both are modeled as the product of a typical length and the velocity scale, namely LU.

The eddy viscosity $\nu_t^{'}$ from the turbulence generated by the ice cover and the channel bed bottom can be defined on the basis of the Elder formulation:

$$\nu_t^{'} = \alpha D(y)\sqrt{c_f}U(y) \tag{7}$$

where α is a constant, $D(y)$ is the local flow depth and used as the length scale, $\sqrt{c_f}U$ is the friction velocity and used as the velocity scale, and c_f is the comprehensive friction coefficient. For the ice-covered compound channels, both the ice cover resistance and the channel bed friction contribute to the comprehensive friction coefficient c_f, which can be derived as (Wang et al., 2020):

$$c_f = \frac{g}{\chi_b + \chi_i}\left[\frac{n_b^{3/2} + \zeta n_i^{3/2}}{(1+\zeta)R_d}\right]^{1/3}\left(\chi_b n_b^{3/2} + \chi_i n_i^{3/2}\right) \tag{8}$$

where χ_b is the dimensionless wetted perimeter of the channel bed per unit width; χ_i is the dimensionless wetted perimeter of the ice cover per unit width; ζ is the ratio of χ_i to χ_b; R_d is the comprehensive hydraulic radius, and $R_d = A / (\chi_b + \chi_i)$.

For the momentum exchange contributed from the horizontal coherent structures, Prandtl's mixing length model is utilized to model the eddy viscosity $\nu_t^{'}$ (van Prooijen et al., 2005):

$$\nu_t^{'} = \frac{D_A}{D(y)}\beta^2\delta^2\left|\frac{dU(y)}{dy}\right| \tag{9}$$

where D_A is the averaged flow depth defined as $D_A = (D_m + D_f)/2$, D_m is the flow depth in the main channel, D_f is the flow depth at the ice-covered floodplain (see Figure 3c), β is a proportional constant, and δ is

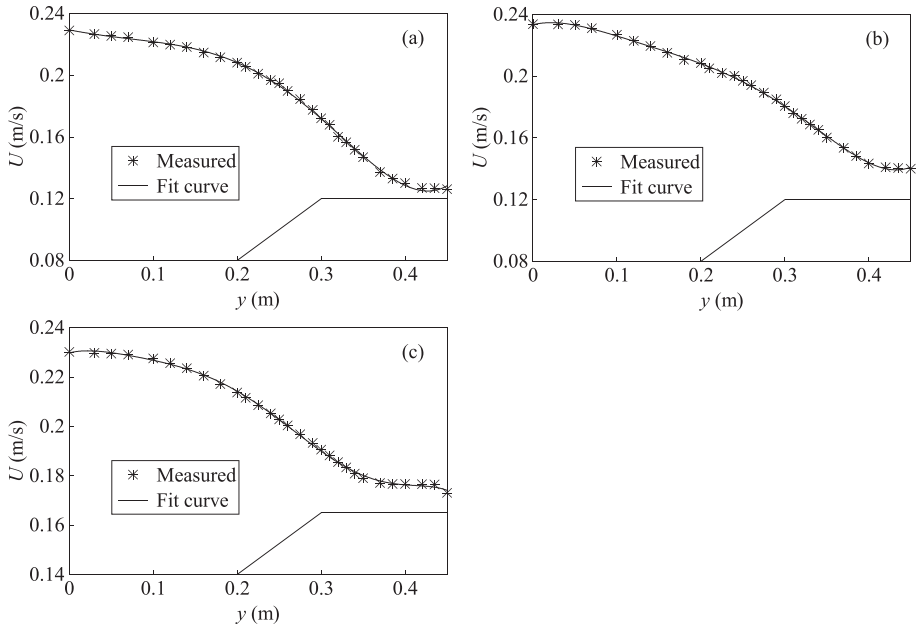

Figure 15. Measured transverse velocity profiles and the corresponding fitted curves. (a) Case I; (b) Case II; (c) Case III.

the mixing layer width. By combining Equation 7 with 9, the eddy viscosity ν_t for the ice-covered compound channel can be written as:

$$\nu_t = \alpha D(y)\left(\frac{g}{\chi_b + \chi_i}\left[\frac{n_b^{3/2} + \zeta n_i^{3/2}}{(1+\zeta)R_d}\right]^{1/3}\left(\chi_b n_b^{3/2} + \chi_i n_i^{3/2}\right)\right)^{1/2} U(y) + \frac{D_A}{D(y)}\beta^2\delta^2\left|\frac{dU(y)}{dy}\right| \quad (10)$$

Substituting Equation 10 into Equation 6 yields a model that can be used to calculate the transverse shear stress for the ice-covered compound channel flows. Moreover, Equation 10 can be also applied to the open compound channel provided that those physical parameters associated with the ice cover are set as zero.

The effectiveness of the eddy viscosity model proposed in this study is evaluated based on the experimental data of this paper. The experimental transverse shear stress is determined by $\overline{T}_{xy-E} = -\rho\overline{u'v'}$. The modeled transverse shear stress is calculated as $\overline{T}_{xy-M} = \rho\nu_t\frac{dU}{dy}$, where ν_t is calculated using Equation 10. To determine ν_t, the velocity gradient and the mixing layer width need to be calculated based on the measured streamwise velocity. To this end, a fifth-order polynomial curve is used to fit the measured streamwise velocities in the representative fully developed cross-section for the three cases, and the results are shown in Figure 15.

Subsequently, the velocity gradient dU/dy and the mixing layer width δ can be calculated according to the related definitions in the previous section. For the open channel flow with a free water surface, the constant α usually has a value of 0.1 (Fischer et al., 1979). For the ice-covered channel flow, however, the presence of the ice cover adds a no-slip boundary, thereby altering the vertical profile of the streamwise velocity. Thus, a two-layer hypothesis is usually used to study the ice-covered channel flow that can be treated as two pseudo-free-surface flows (Sukhodolov et al., 1999; Tsai & Ettema, 1994). Therefore, the constants α for both Cases I and II are set to 0.05, which is equal to half of that of the open channel. The constants β for Cases I and II are set to 0.026 and 0.014, respectively. For Case III (i.e., the open compound channel flow), the constant α is set to 0.1, whereas the constant β is ignored because the horizontal coherent structure is weak. Finally, the eddy viscosity ν_t', ν_t', and ν_t for the three cases can be determined by Equations 7–10. To illustrate the mechanisms responsible for the eddy viscosity, we take the simulated

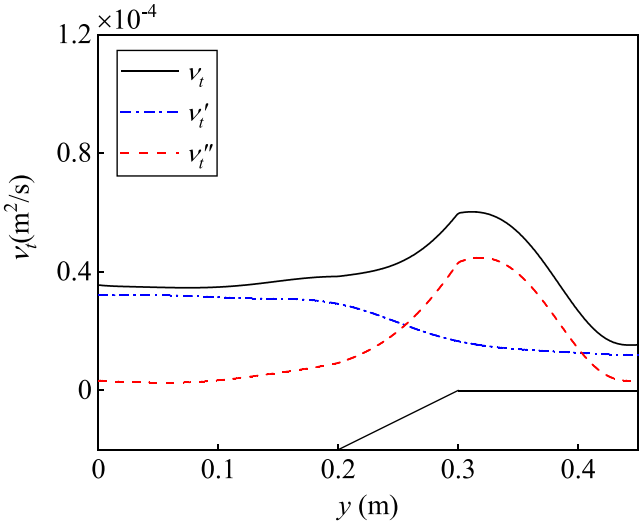

Figure 16. Transverse profile of the eddy viscosity determined by Equations 7–10 for Case I.

results of Case I as an example. As shown in Figure 16, the eddy viscosity generated by the horizontal coherent structure plays a key role in the ice-covered floodplain region, while the eddy viscosity induced by the bottom turbulence dominates in the main channel region. This result coincides with the study of van Prooijen et al. (2005). Thus, according to $\overline{T}_{xy-M} = \rho\nu_t dU / dy$, the modeled transverse shear stress can be obtained.

Figure 17 shows the comparison of the calculated and measured transverse shear stress profiles at the representative fully developed cross-section for the three cases. In general, the calculated transverse shear stresses agree well with the measurements for the three cases, demonstrating the rationalization of the proposed eddy viscosity model. Some deviation between the calculation and measurement exists near the edge of the ice-covered floodplain for Cases I and II. This may be attributed to the neglect of the secondary flow effect on the transverse momentum exchange. Furthermore, the value of β for Case II is relatively small compared with that for Case I, which may be resulted from the relatively weak horizontal coherent structure for Case II. For Case III, the simulated result underestimates the transverse shear stress at the floodplain and side slope regions because the combined effects of the horizontal coherent structure and secondary flow are neglected. Although the simulated results illustrate the effectiveness of the eddy viscosity model, the values of constants α and β presented here are lack of universality due to the limited experimental cases.

5. Discussion

Through laboratory experiments, we have mainly investigated the water flow in the compound channel with the shore ice covered on the floodplain. It has been observed that the longitudinal distance needed for flow to reach the fully developed state decreases with the decrease of the flow depth ratio in the compound channel with the shore ice. This indicates that the small flow depth ratio restricts the evolution of

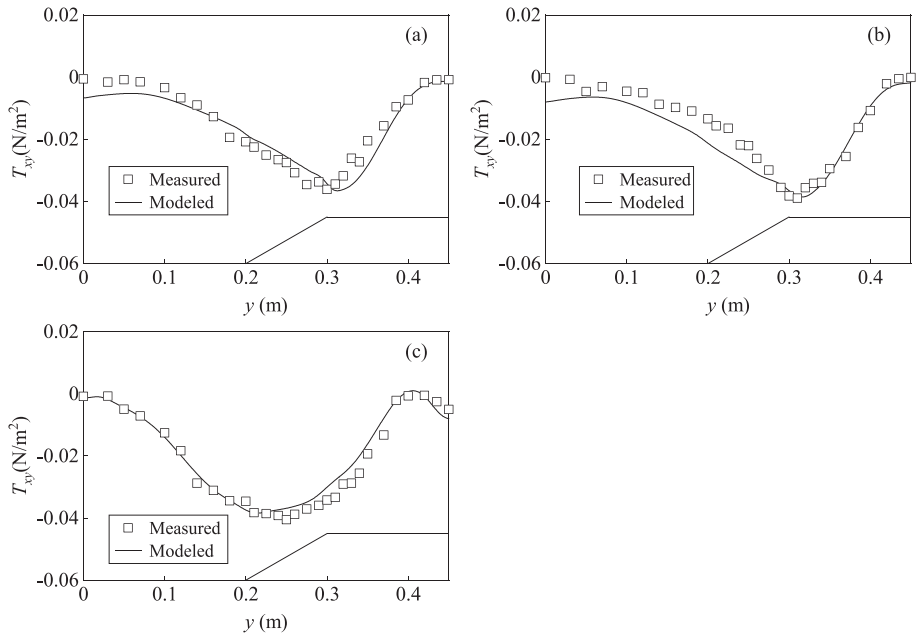

Figure 17. Comparison of the calculated (solid lines) and the measured (open squares) transverse shear stress. (a) Case I; (b) Case II; (c) Case III.

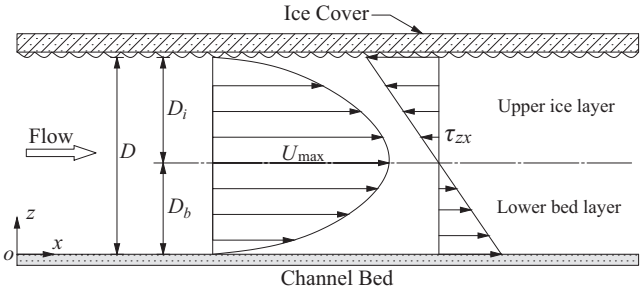

Figure 18. Sketch of vertical profiles of the streamwise velocity U and the turbulent shear stress τ_{zx} in the ice-covered channels.

the water flow. As compared with that of the open compound channel flow, the flow development in the ice-covered compound channel is restricted due to the additional resistance induced by the shore ice (see Figure 4). Besides, whether the floodplain is covered by the shore ice, the longitudinal distance required for flow at the floodplain to realize the fully developed state is longer than that in the main channel. This result may be ascribed to the relatively slow streamwise velocity at the floodplain and is similar to the flow development presented by Bousmar et al. (2005). When water flow reaches the fully developed cross-section, the streamwise velocity in the compound channel with the shore ice is self-similar under different flow depth ratios and a velocity inflection point is detected near the edge of the ice-covered floodplain (see Figure 8). It should be noted that the streamwise velocity outside the floodplain mixing layer for the open compound channel (i.e., Case III) has been affected by the vertical wall boundary resistance. Furthermore, relatively large Reynolds shear stresses are observed within the mixing layer. The position that the maximum Reynolds shear stress occurs coincides with the location of the velocity inflection point for the compound channel with the shore ice, indicating the generation of the coherent vortices that maintain the lateral momentum exchange between the ice-covered floodplain and the main channel. For the open compound channel without shore ice, however, the positions of the maximum Reynolds shear stress and the velocity inflection point deviate from the interface to the side slope. By analyzing the power spectral density of the transverse velocity fluctuation at the edge of the floodplain, it is found that the turbulence inside the vortex center is quasi-periodic and has a quasi-2D coherent structure (see Figure 12). From the quadrant analysis of the Reynolds shear stress, the momentum exchange within the mixing layer is dominated by both the sweep event and the ejection event (see Figure 14). An eddy viscosity model for the ice-covered channel flows is also presented. Though the effectiveness of the eddy viscosity model is validated by comparing with the available experimental data, further experiments with a wide range of flow depth ratios are required to investigate the universal value or range for α and β.

As compared with experimental results of the open compound channel, though the presence of the shore ice has no essential influence on the horizontal coherent structure of the compound channel flow, the shore ice covered on the floodplain will significantly alter the flow characteristics, especially the vertical distributions of the streamwise velocity U and the turbulent shear stress τ_{zx} (See Figure 18). Figure 18 shows that the longitudinal profile of the ice-covered channel flow can be divided into two layers (i.e., the lower bed layer and the upper ice layer) according to Einstein's resistance separation theory (Einstein, 1942). The streamwise velocity U in the ice-covered channel, whose maximum value U_{max} locates at the interface of the two layers, has a similar vertical distribution to that of the pipe turbulent flow. The turbulent shear stress τ_{zx} with a zero value at the interface of the two layers linearly varies in the vertical direction and has opposite signs in the two layers. In the experiment, the vertical distributions of the streamwise velocity U in the open main channel and at the ice-covered floodplain of the cross-section $x = 8$m for Case II are measured and shown in Figure 19. It is seen that the streamwise velocity U of the ice-covered floodplain is distinctly different from that of the open main channel. Furthermore, Lotsari et al. (2019) pointed out that two vertically superimposed helical secondary flow cells can occur under the ice cover and the rotational direction of the secondary flow is opposite to the open channel. Hence, the presence of the shore ice fundamentally changes the flow characteristics of the compound channel, comparing to the normal compound channel with an ice-free surface.

When the quadrant analysis is applied to analyze the transverse momentum exchange, the four quadrants of the u'-v' plane are normally classified as outward interactions (Q1), ejections (Q2), inward interactions (Q3), and sweeps (Q4) (Willmarth & Lu, 1972). In this study, however, the four quadrants are classified as sweeps (Q1), inward interactions (Q2), ejections (Q3), and outward interactions (Q4), which differs from the traditional classification. This can be understood by analyzing the lateral distribution of the streamwise velocity. First of all, we need to know that the motion of the high-momentum fluid toward the boundary corresponds to the sweep event and the motion of the low-momentum fluid from the boundary corresponds to the ejection event (Sukhodolov et al., 1999). As shown in Figure 4, the time-averaged streamwise velocity

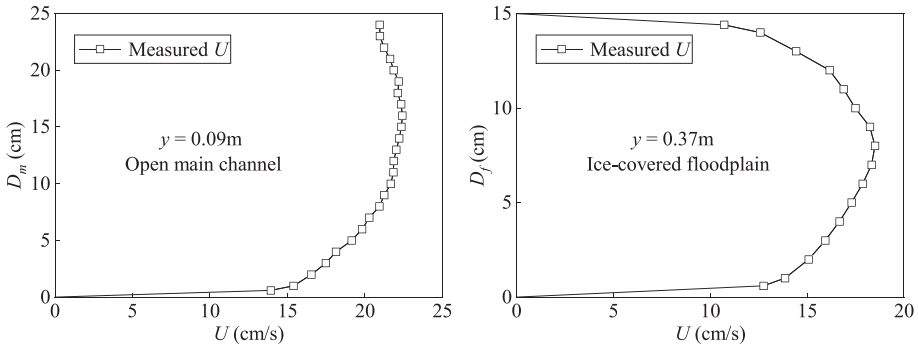

Figure 19. Vertical distribution of measured U at different locations of the cross-section $x = 8$m for Case II.

U actually decreases with the lateral coordinate y. Supposing that there exist two adjacent thin layers paralleling to the x-z plane, that is, the normal directions of the two adjacent thin layers parallel to the lateral direction y. For the sake of simplicity, the two adjacent thin layers are marked as L layer and R layer, the lateral positions of the two layers satisfy $y_L < y_R$, thereby $U_L > U_R$. When a unit water body from the L layer enters into the R layer, it implies that the unit water body has a positive lateral velocity fluctuation (i.e., $v' > 0$). Furthermore, to achieve the momentum exchange between the two layers, the time-averaged streamwise velocity of the unit water body U_L in the L layer will become the instantaneous streamwise velocity in the R layer. Considering that $U_L > U_R$, the streamwise velocity fluctuation of the unit water body in the R layer is positive (i.e., $u' > 0$). Hence, the motion of the unit water body from the L layer into the R layer corresponds to the sweep event that locates at the first quadrant ($u' > 0$, $v' > 0$). Similarly, if a unit water body from the R layer enters into the L layer, its lateral velocity fluctuation is negative (i.e., $v' < 0$), and its streamwise velocity fluctuation in the L layer is negative (i.e., $u' < 0$) because of $u' = U_R - U_L$. In this case, the motion of the unit water body from the R layer into the L layer corresponds to the ejection event that locates at the third quadrant ($u' < 0$, $v' < 0$). Therefore, this is why the classification presented here is different from the traditional classification.

In practice, the roughness of the ice cover changes with different thermal and hydraulic conditions. During the formation and growth of the ice cover, its underside is relatively smooth; whereas the bottom of the ice cover turns to be rippled when the ambient air temperature changes and the water flow temperature is above the freezing point (Lawson et al., 1986). In this study, the simulated ice cover, which can be regarded as the fully growing ice cover, has a constant equivalent roughness height k_s. According to the study of Ackers (1991), Manning's roughness coefficient n was related to the equivalent roughness height k_s, namely $n = k_s^{1/6} / \left(8.25\sqrt{g}\right)$. Considering that both the channel bed and the shore ice for all cases are made up of the same materials, the equivalent roughness heights of the channel bed and the shore ice remain unchanged for all cases tested. Moreover, J.-I. Yoon et al. (2012) investigated the variation of the Manning's roughness coefficient n with the relative flow depth and found that n was nearly constant when the relative flow depth was larger than 50%. Therefore, it is reasonable to assume that the values of n_b and n_i keep constant for all regions and all cases based on the fact that the equivalent roughness height is unchanged and the flow depth ratio is relatively large in the present experiment.

It is worth noting that the additional resistance caused by the shore ice is directly reflected by the friction coefficient. Although Manning's roughness coefficients under different cases remain constant, the friction coefficients c_f for different regions and different cases are different. The reason is that the friction coefficients c_f mainly depend on the hydraulic radius (see Equation 8). Given the roughness of the shore ice and the smaller hydraulic radius of the ice-covered floodplain region, the friction coefficient c_f in the ice-covered floodplain region is larger than that in the open main channel region. Thus, the ice-covered floodplain region will have a relatively great boundary resistance. Meanwhile, the study of Zare et al. (2016) showed that the ratio n_i/n_b could be up to 4.0, which demonstrates the ratio $n_i/n_b = 1.17$ presented in this study is rational. Besides, it should be noted that the water flow in the experiments does not belong to the shallow flow ($D_r < 0.33$) according to the classification of Nezu et al. (1999). The flow depth ratio D_r used in the experiments is relatively large because of the restriction of the laboratory equipment, thereby causing

the inconspicuous horizontal coherent structure to some extent. Further study is required to explore the effect of the varied ice cover roughness on the turbulent structure for the ice-covered compound channel shallow flow.

6. Conclusions

In this paper, the flow velocity field in a symmetric compound channel with and without the shore ice covered on the floodplain is measured under different flow depth ratios. These data are analyzed to investigate the turbulence structure and the transverse momentum exchange between the ice-covered floodplain and the main channel. The presence of the shore ice results in additional friction on the floodplain domain, thereby forming a discontinuous frictional resistance across the cross-section. The main results obtained from this study are summarized as follows:

(i) Whether the floodplain is covered by the shore ice, the streamwise velocities have a similar evolution trend. Specifically, before realizing the fully developed state, the streamwise velocity in the main channel increases with the increase of downstream distance, while the streamwise velocity on the floodplain decreases downstream. Meanwhile, a velocity inflection point appears in the transverse profile of the streamwise velocity near the interface between the main channel and the floodplain. Two mixing layer widths (i.e., δ_m in the main channel and δ_f over the floodplain) on both sides of the velocity inflection point exhibit an increasing trend and then tend to be stable at different longitudinal positions, which is consistent with the development process of the streamwise velocity. Nevertheless, the shore ice resistance reduces the downstream distance required to reach the fully developed state and induces a relatively strong mixing shear layer near the edge of the ice-covered floodplain.

(ii) For the compound channel with the shore ice, as water flow reaches the fully developed zone, both the velocity inflection point and the maximum Reynolds shear stress occur at the interface between the ice-covered floodplain and the main channel, which implies the generation of the coherent vortices. For the open compound channel, however, the maximum Reynolds shear stress and the velocity inflection point diverge from the interface to the side slope, which may be ascribed to the relatively large flow depth ratio and the lack of shore ice suppression. The power spectral density analysis shows that the coherent vortices have a quasi-2D turbulence coherent structure and oscillate around a single dominant frequency. The dominant frequency of the turbulent vortex in the compound channel with the shore ice is slightly greater than that in the open compound channel. The quasi-periodic oscillation is maintained by a circulation composed of sweeps and ejections. Sweeps transport the high-momentum fluid across the interface to the ice-covered floodplain, enhancing the velocity gradient and generating high local energy. Ejections subsequently convey the high-momentum fluid from near the interface back into the main channel. Thus, the transverse momentum exchange between the ice-covered floodplain and the main channel is achieved under the combined action of the ejection and sweep motions.

(iii) To model the transverse momentum exchange, based on the previous studies, we present an eddy viscosity model that contains the turbulence generated underneath the ice cover. On the whole, the simulated transverse shear stress agrees well with the measurements, which verifies the effectiveness of the eddy viscosity model. However, considering that the ice-covered channel flow is usually treated as two pseudo-free-surface flows, the constant α presented here is half of the commonly used value in the open compound channel. Moreover, the value of the constant β is given after matching the simulated results with measured results, which lacks universality. Hence, further experiments under the ice cover with wide flow conditions are required to investigate the universal value or range for α and β in the eddy viscosity model.

Although this study investigates the turbulent structure for straight ice-covered compound channel flows, the experiments are performed with relatively large flow depth ratios due to the limitation of the laboratory equipment. Therefore, further studies should take into account the small flow depth ratio as well as the flow characteristics of the curved ice-covered compound channel flows.

Appendix A

When we conduct velocity measurements in the compound channel with the shore ice, the time-averaged streamwise velocity measured at the water level corresponding to the four-fifths of the floodplain flow depth (denoted by $U_{4d/5}$) is utilized to represent the depth-averaged streamwise velocity U_d. To demonstrate the feasibility of this measurement scheme, an additional experiment with $Q = 0.0411$ m^3/s and $D_f = 0.15$ m is performed along the cross-section $x = 8$m in the compound channel with the ice-covered floodplains. Twenty-two vertical lines are arranged over the cross-section. Each vertical line in the main channel has at least 20 measurement points, while 15 measurement points are considered in each vertical line of the ice-covered floodplain. The experimental results are shown in Figure A1a. It is seen that $U_{4d/5}$ is approximately equal to U_d. The relative error between the measured $U_{4d/5}$ and U_d is calculated by $\left|U_d - U_{4d/5}\right| / U_d \times 100\%$. Figure A1b plots the relative error, showing that all relative errors are smaller than 10% with a maximum value of 9.72%. The averaged relative error between $U_{4d/5}$ and U_d is 3.51%, demonstrating the rationalization of replacing U_d with $U_{4d/5}$.

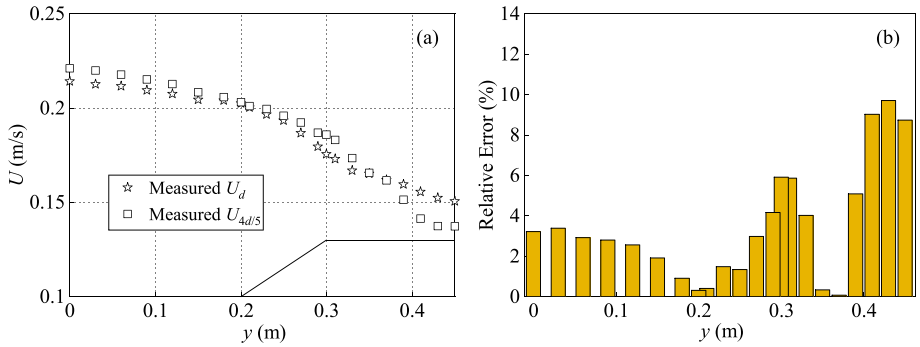

Figure A1. Experimental results measured at the cross-section $x = 8$m in the compound channel with the shore ice. (a) Lateral profiles of the measured U_d and $U_{4d/5}$; (b) Relative errors of the measured $U_{4d/5}$ against the measured U_d.

Nomenclature

A	Cross-section area (m^2)
B_f	Width of the floodplain (m)
B_m	Half the width of the main channel (m)
c_f	Comprehensive friction coefficient (−)
D	Bankfull height of the main channel (m)
D_A	Averaged flow depth (m)
D_f	Flow depth on the ice-covered floodplain (m)
D_m	Flow depth in the main channel (m)
D_r	Flow depth ratio (−)
D_b	Flow depth of the lower bed layer (m)
D_i	Flow depth of the upper ice layer (m)
Fr	Froude number (−)
g	Gravitational acceleration (m/s^2)
H	Threshold value (−)
n_b	Manning's roughness coefficient of channel bed (−)
n_i	Manning's roughness coefficient of ice cover (−)
Q	Discharge (m^3/s)
Re	Reynolds number (−)
R_d	Comprehensive hydraulic radius (m)
s	Side slope of the main channel (−)

$S_{i,H}$	Contribution value in the ith quadrant (m^2/s^2)
S_0	Channel bed slope (−)
S_{yy}	Power spectral density ($cm^2/s^2/Hz$)
$\overline{T_{xy}}$	Time-averaged transverse shear stress (N/m^2)
u, v, w	Instantaneous velocity components in x, y, and z directions (m/s)
U, V, W	Time-averaged velocities in x, y, and z directions (m/s)
u', v', w'	Instantaneous velocity fluctuations in x, y, and z directions (m/s)
U_B	Longitudinal bulk flow velocity (m/s)
U_d	Depth-averaged streamwise velocity (m/s)
ν	Water kinematic viscosity (m^2/s)
υ_t	Eddy viscosity (m^2/s)
υ_t'	Eddy viscosity from turbulence generated by the ice cover and the bed bottom(m^2/s)
υ_t'	Eddy viscosity from horizontal coherent structures (m^2/s)
x, y, z	Longitudinal, lateral, and vertical directions (−)
χ	Cross-section wetted perimeter (m)
τ_{zx}	Turbulent shear stress (N/m^2)
δ	Mixing layer width (cm)
θ	Momentum thickness (cm)

Data Availability Statement

All the data used in this study are available through https://zenodo.org/record/3992412#.Xz3ZzWgzaUk. The data about the depth-averaged streamwise velocity used in Figure A1 have been reported by Wang et al. (2020).

Acknowledgments
This research was supported by the National Natural Science Foundation of China (grant numbers 52020105006 and 11872285) and the Open Funding of State Key Laboratory of Water Resources and Hydropower Engineering Science (WRHES), Wuhan University (Project number 2018HLG01). We are grateful to Zhiming Yuan and Ran Chen for providing the photos shown in Figure 1. Comments made by reviewers have significantly improved the quality of the paper.

References

Ackers, P. (1991). Hydraulic design of straight compound channels. In *Detailed development of design method* (Vol. 2). HR Wallingford.
Alaee, M. J., Pattiaratchi, C., & Ivey, G. (2007). Numerical simulation of the summer wake of Rottnest Island, Western Australia. *Dynamics of Atmospheres and Oceans*, *43*(3–4), 171–198. https://doi.org/10.1016/j.dynatmoce.2007.01.001
Biron, P. M., Buffin-Bélanger, T., & Martel, N. (2019). Three-dimensional turbulent structures at a medium-sized confluence with and without an ice cover. *Earth Surface Processes and Landforms*, *44*(15), 3042–3056. https://doi.org/10.1002/esp.4718
Bousmar, D., Rivière, N., Proust, S., Paquier, A., Morel, R., & Zech, Y. (2005). Upstream discharge distribution in compound-channel flumes. *Journal of Hydraulic Engineering*, *131*(5), 408–412. https://doi.org/10.1061/(asce)0733-9429(2005)131:5(408)
Chand, K., Sharma, M., Vishnu, V. T., & De, A. K. (2019). Statistics of coherent structures in two-dimensional turbulent Rayleigh-Bénard convection. *Physics of Fluids*, *31*(11), 115112. https://doi.org/10.1063/1.5125758
Chow, V. T. (1959). *Open channel hydraulics*. McGraw Hill.
Demers, S., Buffin-Bélanger, T., & Roy, A. G. (2013). Macroturbulent coherent structures in an ice-covered river flow using a pulse-coherent acoustic Doppler profiler. *Earth Surface Processes and Landforms*, *38*(9), 937–946. https://doi.org/10.1002/esp.3334
Dupuis, V., Proust, S., Berni, C., & Paquier, A. (2017). Mixing layer development in compound channel flows with submerged and emergent rigid vegetation over the floodplains. *Experiments in Fluids*, *58*(4), 30. https://doi.org/10.1007/s00348-017-2319-9
Einstein, H. A. (1942). Formulas for the transportation of bed-load. *Transactions of ASCE*, *107*(2140), 561–597. https://doi.org/10.1061/taceat.0005468
Ettema, R. (2002). Review of alluvial-channel responses to river ice. *Journal of Cold Regions Engineering*, *16*(4), 191–217. https://doi.org/10.1061/(asce)0887-381x(2002)16:4(191)
Ettema, R., & Zabilansky, L. (2004). Ice influences on channel stability: Insights from Missouri's Fort Peck reach. *Journal of Hydraulic Engineering*, *130*(4), 279–292. https://doi.org/10.1061/(asce)0733-9429(2004)130:4(279)
Fernandes, J. N., Leal, J. B., & Cardoso, A. H. (2014). Improvement of the lateral distribution method based on the mixing layer theory. *Advances in Water Resources*, *69*, 159–167. https://doi.org/10.1016/j.advwatres.2014.04.003
Fischer, H. B., List, E. J., Koh, R. C. Y., Imberger, J., & Brooks, N. H. (1979). *Mixing in inland and coastal waters*. Academic.
Goring, D. G., & Nikora, V. I. (2002). Despiking acoustic Doppler velocimeter data. *Journal of Hydraulic Engineering*, *128*(1), 117–126. https://doi.org/10.1061/(asce)0733-9429(2002)128:1(117)
Guo, J. K., Shan, H. Y., Xu, H. J., Bai, Y. C., & Zhang, J. M. (2017). Exact solution for asymmetric turbulent channel flow with applications in ice-covered rivers. *Journal of Hydraulic Engineering*, *143*(10), 04017041. https://doi.org/10.1061/(asce)hy.1943-7900.0001360
Hoque, M. A. (2009). *Hydraulic analysis of ice-covered river flow (Master's thesis)*. Concordia University. Retrieved from ProQuest https://search.proquest.com/docview/597918590/2FFF03E6C78453DPQ/1?accountid=15157
Juez, C., Schärer, C., Jenny, H., Schleiss, A. J., & Franca, M. J. (2019). Floodplain land cover and flow hydrodynamic control of overbank sedimentation in compound channel flows. *Water Resources Research*, *55*(11), 9072–9091. https://doi.org/10.1029/2019wr024989
Kirillin, G., Leppäranta, M., Terzhevik, A., Granin, N., Bernhardt, J., Engelhardt, C., et al. (2012). Physics of seasonally ice-covered lakes: A review. *Aquatic Sciences*, *74*(4), 659–682. https://doi.org/10.1007/s00027-012-0279-y

Lawson, D. E., Chacho, E. F., Brockett, B. E., Wuebben, J. L., Collins, C. M., Arcone, S. A., & Delaney, A. J. (1986). *Morphology, hydraulics and sediment transport of an ice-covered river: Field techniques and initial data (CRREL Report 86-11)*. Hanover, NH: U.S. Army Cold Regions Research and Engineering Laboratory.

Liu, C., Luo, X., Liu, X., & Yang, K. (2013). Modeling depth-averaged velocity and bed shear stress in compound channels with emergent and submerged vegetation. *Advances in Water Resources*, *60*, 148–159. https://doi.org/10.1016/j.advwatres.2013.08.002

Lotsari, E., Tarsa, T., Kämäri, M., Alho, P., & Kasvi, E. (2019). Spatial variation of flow characteristics in a subarctic meandering river in ice-covered and open-channel conditions: A 2D hydrodynamic modeling approach. *Earth Surface Processes and Landforms*, *44*(8), 1509–1529. https://doi.org/10.1002/esp.4589

Lu, S. S., & Willmarth, W. W. (1973). Measurements of the structure of the Reynolds stress in a turbulent boundary layer. *Journal of Fluid Mechanics*, *60*(3), 481–511. https://doi.org/10.1017/s0022112073000315

Morse, B., & Hicks, F. (2005). Advances in river ice hydrology 1999-2003. *Paper presented at Annual Hydrology Session Meeting of the Canadian-Geophysical-Union, Canadian Geophysical Union, Hydrology Section, Banff, Canada*. https://doi.org/10.1002/hyp.5768

Muste, M., Braileanu, F., & Ettema, R. (2000). Flow and sediment transport measurements in a simulated ice-covered channel. *Water Resources Research*, *36*(9), 2711–2720. https://doi.org/10.1029/2000wr900168

Namaee, M. R., & Sui, J. Y. (2019). Effects of ice cover on the incipient motion of bed material and shear stress around side-by-side bridge piers. *Cold Regions Science and Technology*, *165*. UNSP 102811. https://doi.org/10.1016/j.coldregions.2019.102811

Nezu, I., Onitsuka, K., & Iketani, K. (1999). *Hydraulic modeling* (pp. 17–32). Water Resources Publications.Coherent horizontal vortices in compound open channel flows

Patel, M., & Kumar, B. (2017). Flow and bedform dynamics in an alluvial channel with downward seepage. *Catena*, *158*, 219–234. https://doi.org/10.1016/j.catena.2017.07.009

Peters, M., Dow, K., Clark, S. P., Malenchak, J., & Danielson, D. (2017). Experimental investigation of the flow characteristics beneath partial ice covers. *Cold Regions Science and Technology*, *142*, 69–78. https://doi.org/10.1016/j.coldregions.2017.07.007

Proust, S., Fernandes, J. N., Leal, J. B., Rivière, N., & Peltier, Y. (2017). Mixing layer and coherent structures in compound channel flows: Effects of transverse flow, velocity ratio, and vertical confinement. *Water Resources Research*, *53*(4), 3387–3406. https://doi.org/10.1002/2016wr019873

Proust, S., & Nikora, V. I. (2020). Compound open-channel flows: effects of transverse currents on the flow structure. *Journal of Fluid Mechanics*, *885*, A24. https://doi.org/10.1017/jfm.2019.973

Ren, K., Wu, G. X., & Li, Z. F. (2020). Hydroelastic waves propagating in an ice-covered channel. *Journal of Fluid Mechanics*, *886*, A18. https://doi.org/10.1017/jfm.2019.1042

Robert, A., & Tran, T. (2012). Mean and turbulent flow fields in a simulated ice-covered channel with a gravel bed: Some laboratory observations. *Earth Surface Processes and Landforms*, *37*(9), 951–956. https://doi.org/10.1002/esp.3211

Sanjou, M., & Nezu, I. (2009). Turbulence structure and coherent motion in meandering compound open-channel flows. *Journal of Hydraulic Research*, *47*(5), 598–610. https://doi.org/10.3826/jhr.2009.3485

Shiono, K., & Knight, D. W. (1991). Turbulent open-channel flows with variable depth across the channel. *Journal of Fluid Mechanics*, *222*, 617–646. https://doi.org/10.1017/s0022112091001246

Smith, B. T., & Ettema, R. (1997). Flow resistance in ice-covered alluvial channels. *Journal of Hydraulic Engineering*, *123*(7), 592–599592. https://doi.org/10.1061/(asce)0733-9429(1997)123:7(592)

Sukhodolov, A., Thiele, M., Bungartz, H., & Engelhardt, C. (1999). Turbulence structure in an ice-covered, sand-bed river. *Water Resources Research*, *35*(3), 889–894. https://doi.org/10.1029/1998wr900081

Teal, M. J., Ettema, R., & Walker, J. F. (1994). Estimation of mean flow velocity in ice-covered channels. *Journal of Hydraulic Engineering*, *120*(12), 1385–1400. https://doi.org/10.1061/(asce)0733-9429(1994)120:12(1385)

Truong, S. H., & Uijttewaal, W. S. J. (2019). Transverse momentum exchange induced by large coherent structures in a vegetated compound channel. *Water Resources Research*, *55*(1), 589–612. https://doi.org/10.1029/2018wr023273

Tsai, W. F., & Ettema, R. (1994). Modified Eddy viscosity model in fully developed asymmetric channel flows. *Journal of Engineering Mechanics*, *120*(4), 720–732. https://doi.org/10.1061/(asce)0733-9399(1994)120:4(720)

Uijttewaal, W. S. J., & Booij, R. (2000). Effects of shallowness on the development of free-surface mixing layers. *Physics of Fluids*, *12*(2), 392–402. https://doi.org/10.1063/1.870317

van Prooijen, B. C., Battjes, J. A., & Uijttewaal, W. S. J. (2005). Momentum exchange in straight uniform compound channel flow. *Journal of Hydraulic Engineering*, *131*(3), 175–183. https://doi.org/10.1061/(asce)0733-9429(2005)131:3(175)

Wang, F., Huai, W., Liu, M., & Fu, X. (2020). Modeling depth-averaged streamwise velocity in straight trapezoidal compound channels with ice cover. *Journal of Hydrology*, *585*, 124336. https://doi.org/10.1016/j.jhydrol.2019.124336

Wazney, L., Clark, S. P., Malenchak, J., Knack, I., & Shen, H. T. (2019). Numerical simulation of river ice cover formation and consolidation at freeze-up. *Cold Regions Science and Technology*, *168*, UNSP102884. https://doi.org/10.1016/j.coldregions.2019.102884

White, B. L., & Nepf, H. M. (2007). Shear instability and coherent structures in shallow flow adjacent to a porous layer. *Journal of Fluid Mechanics*, *593*, 1–32. https://doi.org/10.1017/s0022112007008415

Willmarth, W. W., & Lu, S. S. (1972). Structure of the Reynolds stress near the wall. *Journal of Fluid Mechanics*, *55*(1), 65–92. https://doi.org/10.1017/s002211207200165x

Xia, X., & Shen, H. T. (2002). Nonlinear interaction of ice cover with shallow water waves in channels. *Journal of Fluid Mechanics*, *467*, 259–268. https://doi.org/10.1017/s0022112002001477

Yoon, J.-I., Sung, J., & Ho Lee, M. (2012). Velocity profiles and friction coefficients in circular open channels. *Journal of Hydraulic Research*, *50*(3), 304–311. https://doi.org/10.1080/00221686.2012.673745

Yoon, J. Y., Patel, V. C., & Ettema, R. (1996). Numerical model of flow in ice-covered channel. *Journal of Hydraulic Engineering*, *122*(1), 19–26.19. https://doi.org/10.1061/(asce)0733-9429(1996)122:1(19)

Yuan, S., Tang, H., Xiao, Y., Qiu, X., Zhang, H., & Yu, D. (2016). Turbulent flow structure at a 90-degree open channel confluence: Accounting for the distortion of the shear layer. *Journal of Hydro-Environment Research*, *12*, 130–147. https://doi.org/10.1016/j.jher.2016.05.006

Zare, S. G. A., Moore, S. A., Rennie, C. D., Seidou, O., Ahmari, H., & Malenchak, J. (2016). Estimation of composite hydraulic resistance in ice-covered alluvial streams. *Water Resources Research*, *52*(2), 1306–1327. https://doi.org/10.1002/2015WR018096

Zhang, J.-x., Wang, J., Fan, X., & Liang, D. (2019). Detached-eddy simulation of turbulent coherent structures around groynes in a trapezoidal open channel. *Journal of Hydrodynamics*, *32*(2), 326–336. https://doi.org/10.1007/s42241-019-0077-2

Zhong, Y., Huai, W. X., & Chen, G. (2019). Analytical model for lateral depth-averaged velocity distributions in rectangular ice-covered channels. *Journal of Hydraulic Engineering*, *145*(1), 04018080. https://doi.org/10.1061/(asce)hy.1943-7900.0001557